Poster presented at the workshop
"Theory and tests of convective energy transport"
Granada, Spain, September 30 – October 2, 1998

A calibration of the mixing-length for solar-type stars based on hydrodynamical simulations of the surface layers

Hans-Günter Ludwig[1], Bernd Freytag[1], & Matthias Steffen[2]

[1]Astronomical Observatory, NBIfAFG, Juliane Maries Vej 30, 2100 Copenhagen Ø, Denmark, [hgl@astro.ku.dk], [bf@astro.ku.dk]
[2]Astrophysikalisches Institut Potsdam, 14482 Potsdam, Germany, [MSteffen@aip.de]

Abstract

We present a grid of numerical 2D radiation hydrodynamics (RHD) models of the solar-like surface convection zones of stars in a wide range of
effective temperatures ($4300\,\mathrm{K} \leq T_{\mathrm{eff}} \leq 7100\,\mathrm{K}$),
gravities ($2.54 \leq \log g \leq 4.74$),
and metallicities ([M/H]=0.0, -0.5, -1.0, -2.0).

We calibrate the free parameter α of the mixing-length theory (MLT) and of two variants of the Canuto-Mazzitelli theory (CMT) to give the same convective efficiency as the RHD models. None of these three 1D descriptions of convection is able to reproduce the results of the RHD simulations with the same parameter α for all combinations of $T_{\mathrm{eff}}/\log g/$[M/H] (Fig. 6 to 20). Nevertheless, the RHD results show no drastic deviations from the range of convective efficiencies assessed from the three simple convection theories.

Applications of the grid of hydrodynamical models concern:
Globular cluster isochrones (⇒ poster 3 by Freytag et al.)
Convection and eclipsing binaries (⇒ poster 33 by Ludwig & Salaris)
Balmer line formation (⇒ poster 17 by Steffen & Ludwig)

1 Numerical simulations

Based on 2D numerical radiation hydrodynamics calculations of time-dependent compressible convection, a variety of stellar surface convection zones has been studied. The equation of state accounts for the ionization of H and He. The non-local equation of radiative energy transport is solved along a number of representative rays, assuming LTE. Grey or frequency-dependent opacities can be used (for details see Ludwig, Jordan, Steffen, 1994, A&A 284, 105).

Models with solar-like deep convection zones need a sophisticated open lower boundary condition that allows the free in- and outflow of material. The inward mass flux is adjusted to keep the mass inside the model constant and the entropy of the inflowing material is regulated as to keep the long-term average of the total radiative flux at the top equal to $\sigma T_{\rm eff}{}^4$.

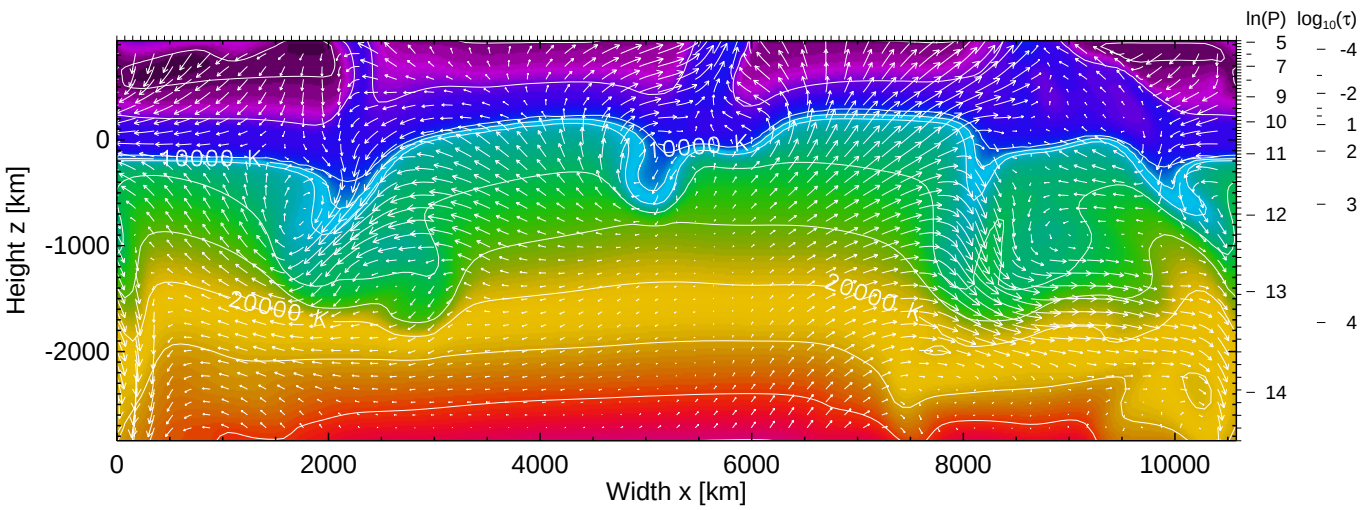

Figure 1: Snapshot of a main-sequence F star model (gt70g44n2) with $T_{\rm eff}$=7 000 K, log$g$=4.44, [M/H]=0.0, 142×71 grid points, $v_{\rm max}$∼18 km/s. Only the upper part of the convection zone is contained in the computational volume.

2 Flow fields

Typical examples of flow patterns are presented in Figs. 1 to 4. The velocity field is indicated by short pseudo-streamlines. Contour lines and colour indicate the temperature T, small tick marks at the top and the right show the positions of the computational grid points. Two columns at the right show some horizontally averaged quantities: the natural logarithm of the mean gas pressure and the logarithm of the optical depth. The origin of the height scale on the left corresponds to the layer with $\log \tau$=0. The height z is counted upward. The lower boundary is open. The top is always transmitting for waves. The lateral boundary conditions are periodic. Grey opacities are used.

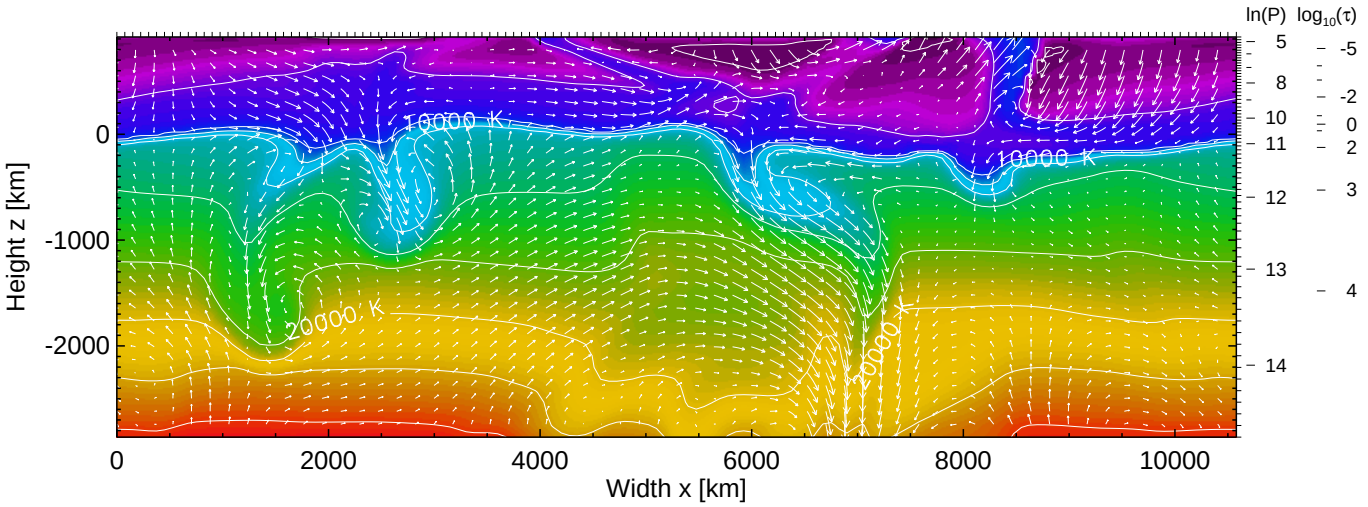

Figure 2: Snapshot of a main-sequence F star model (mt70g44n1) with $T_{\rm eff}$=7 000 K, log$g$=4.44, [M/H]=-0.5, 142×71 grid points, $v_{\rm max}\sim19$ km/s.

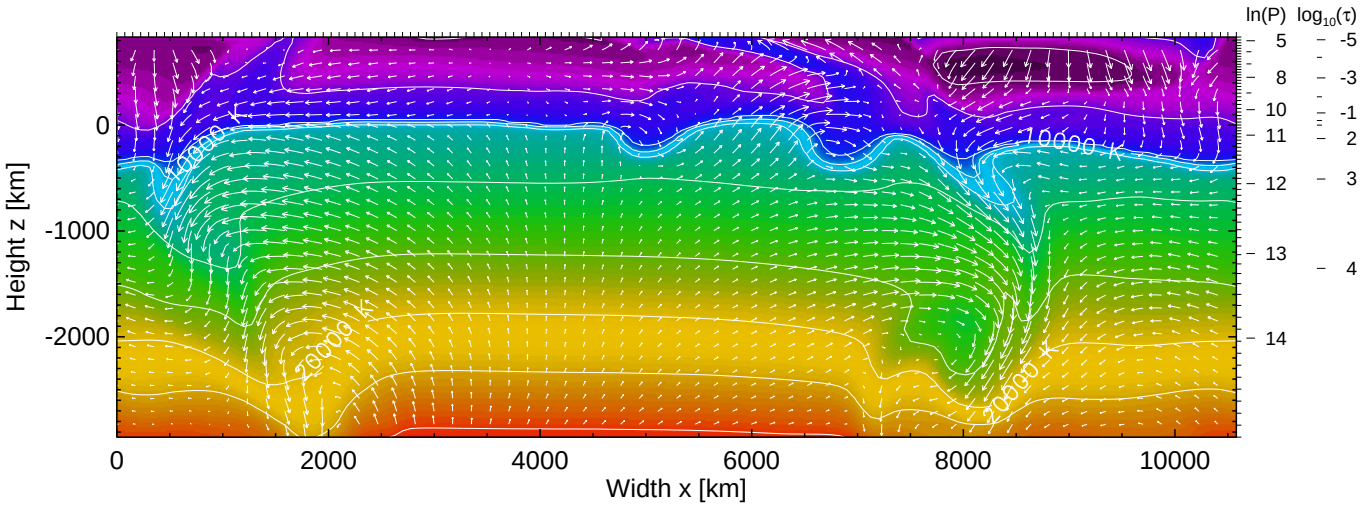

Figure 3: Snapshot of a main-sequence F star model (nt70g44n1) with $T_{\rm eff}$=7 000 K, log$g$=4.44, [M/H]=-1.0, 142×71 grid points, $v_{\rm max}\sim16$ km/s.

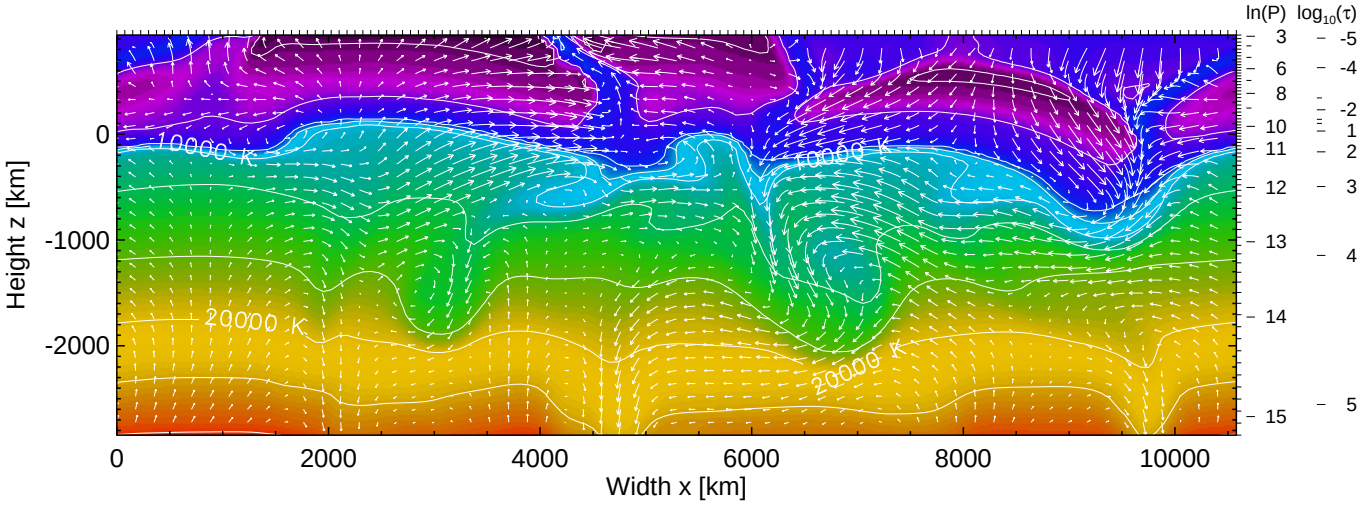

Figure 4: Snapshot of a main-sequence F star model (ot70g44n1) with $T_{\rm eff}$=7 000 K, log$g$=4.44, [M/H]=-2.0, 142×71 grid points, $v_{\rm max}\sim20$ km/s.

3 The entropy of the adiabatically stratified layers ..... ⇒

A direct result of a RHD simulation run is the entropy s^* of the inflowing material which gives the desired total radiative flux at the top. This entropy can be directly identified with the entropy of the deeper, adiabatically stratified layers. In Figs. 5, 7, 9, 11 this entropy is plotted in the $T_{\rm eff}/\log g$ plane for every RHD model for the four metallicities considered, together with contour lines of an analytical fit function to these values.

This entropy shows a rather regular behaviour with little qualitative differences between the four metallicities.

4 Mixing-length theory with $\ell{=}\alpha H_p$ ..... ⇒

The free parameter α describing the mixing-length $\ell{=}\alpha H_p$ is adjusted to produce MLT envelope models with an entropy of the adiabatic layers corresponding to the entropy s^* of the RHD models. In this way an effective mixing-length parameter α is derived (see Steffen, 1993, in "Inside the stars", IAU Coll. 137, eds. Weiss, Baglin, ASPCS 40, 300) for each $T_{\rm eff}/\log g/$[M/H] combination and plotted in Figs. 6, 8, 10, 12 together with a polynomial fit.

For solar metallicity the parameter α shows an increase with falling effective temperature and only a slight dependence on gravity. In the main-sequence phase the effective α for the Sun is a constant close to 1.60. But it increases slightly during the evolution towards the red giant branch (upper right).

For lower metallicities the mixing-length parameter shows a similar decrease towards higher effective temperatures and additionally a drop towards low effective temperatures and high gravities.

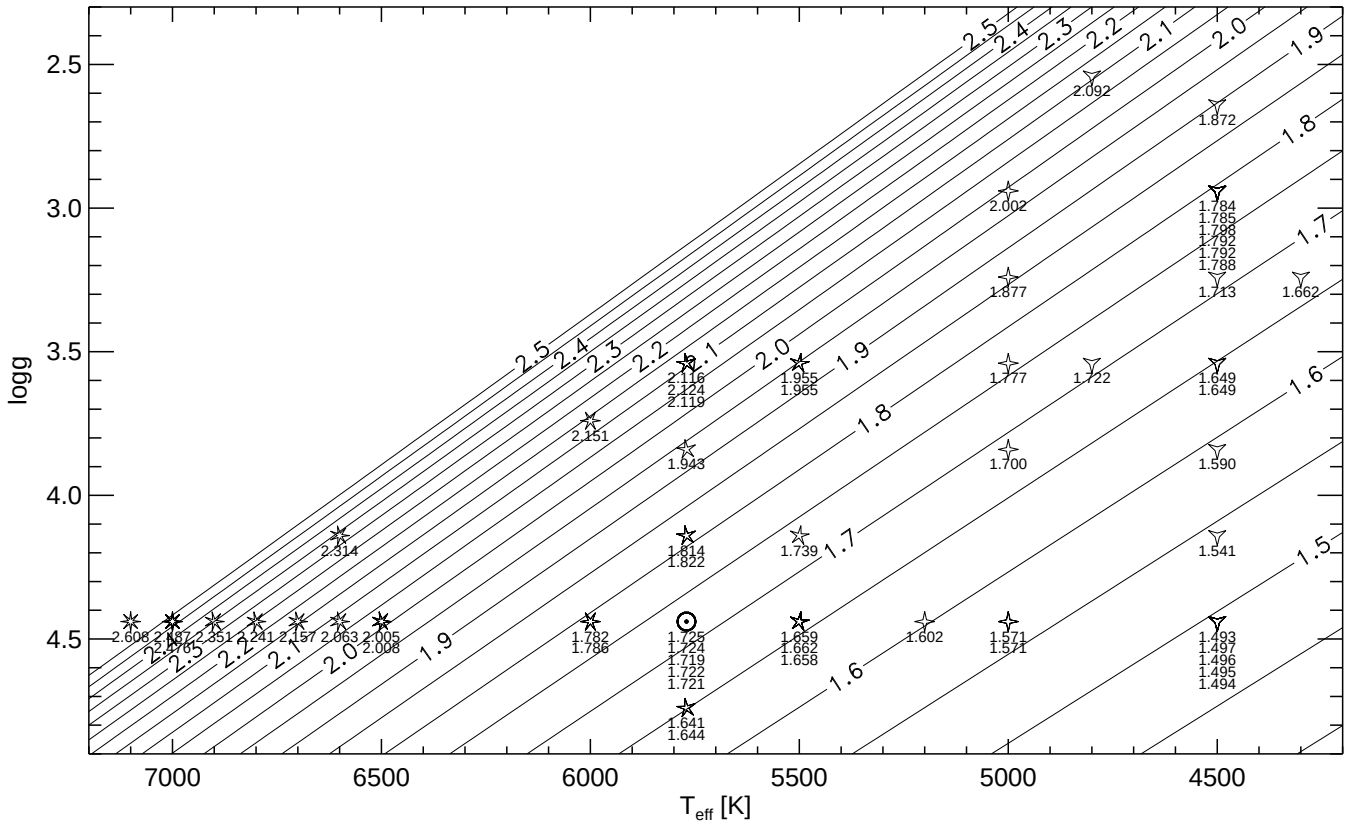

Figure 5: Entropy s^* of the adiabatic layers for solar composition [M/H]=0.0 as function of effective temperature $T_{\rm eff}$ and gravity log$g$. Each symbol indicates one RHD $T_{\rm eff}$/log$g$ parameter set. Every number is the result of a RHD model. The Sun is marked by $\odot$.

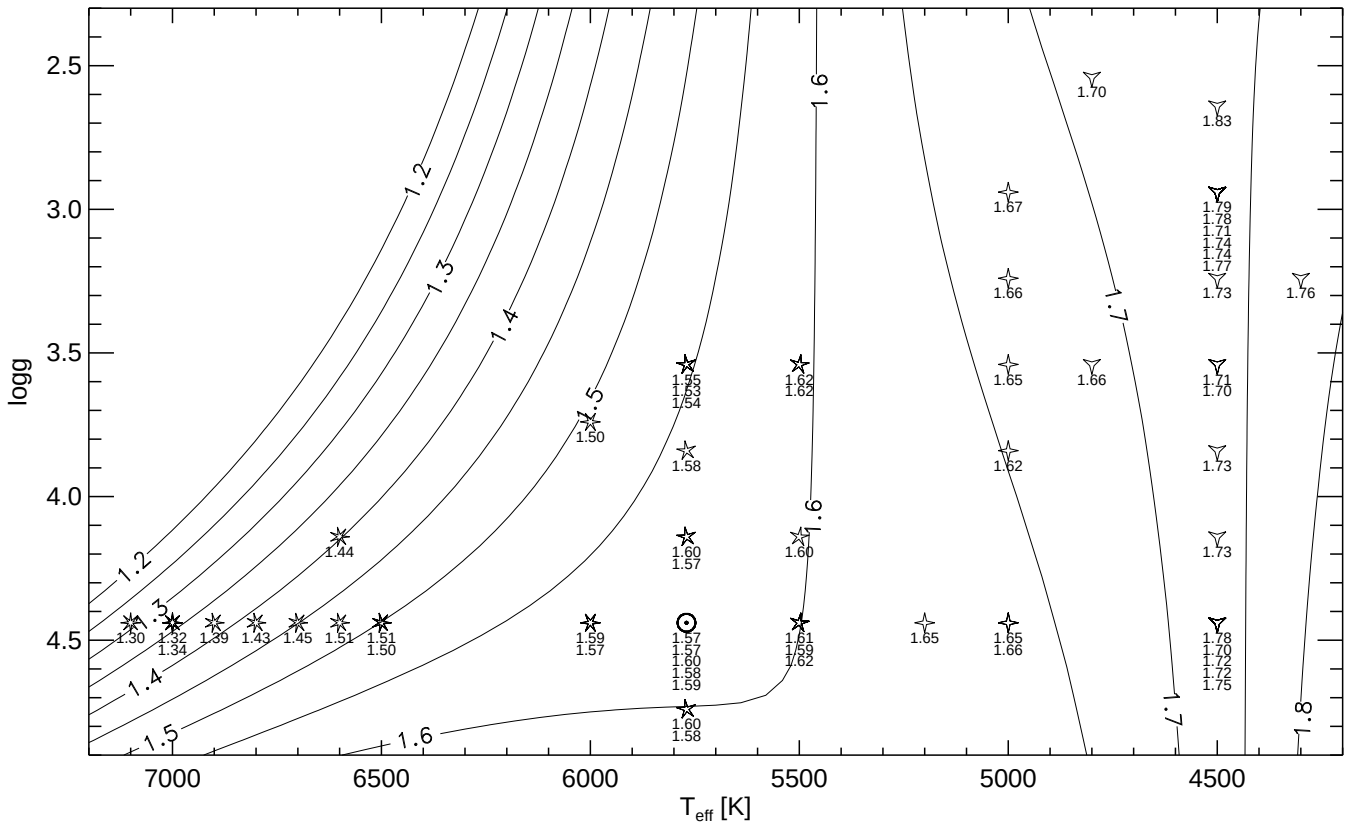

Figure 6: Calibrated parameter α for standard MLT for [M/H]=0.0 as function of effective temperature $T_{\rm eff}$ and gravity log$g$.

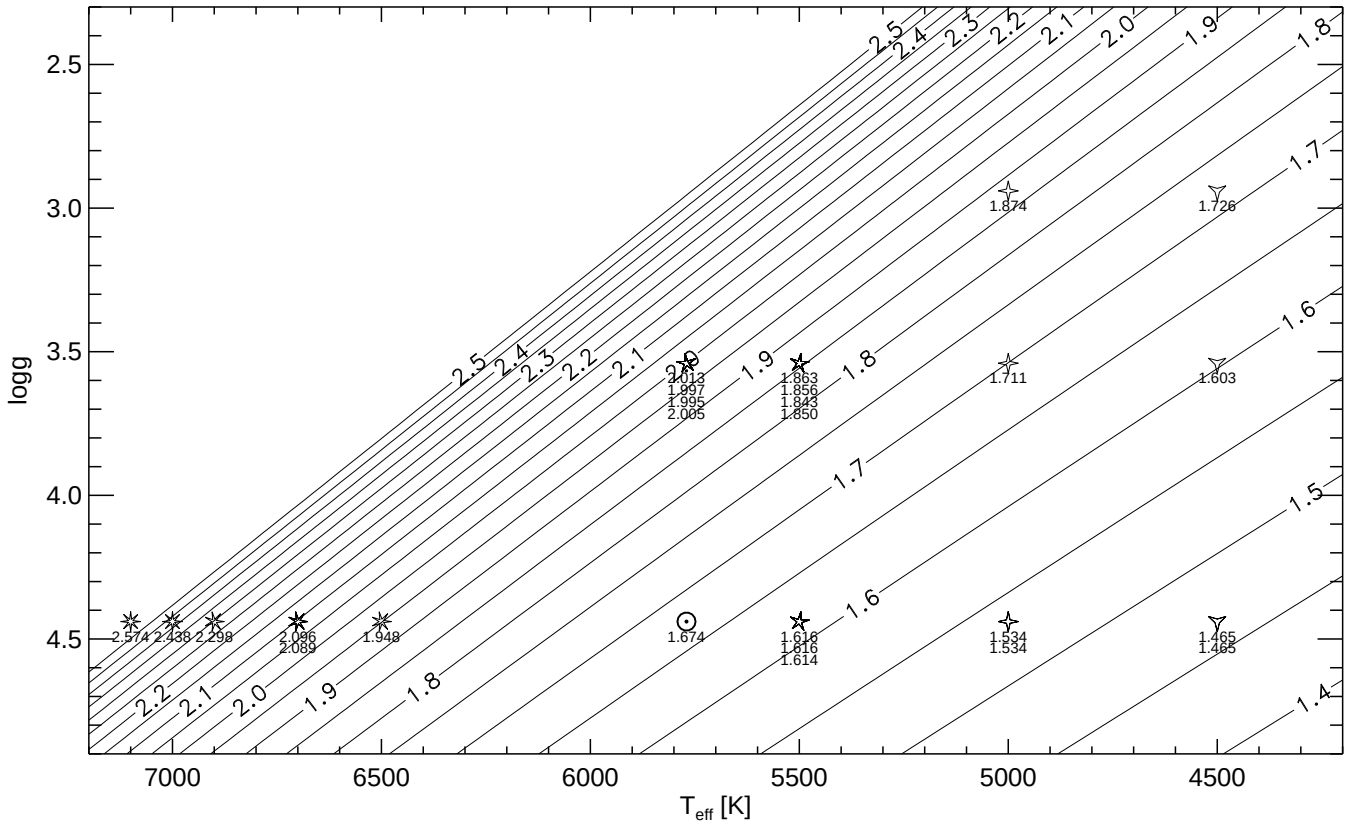

Figure 7: Entropy s^* of the adiabatic layers for [M/H]=-0.5 as function of effective temperature $T_{\rm eff}$ and gravity log$g$.

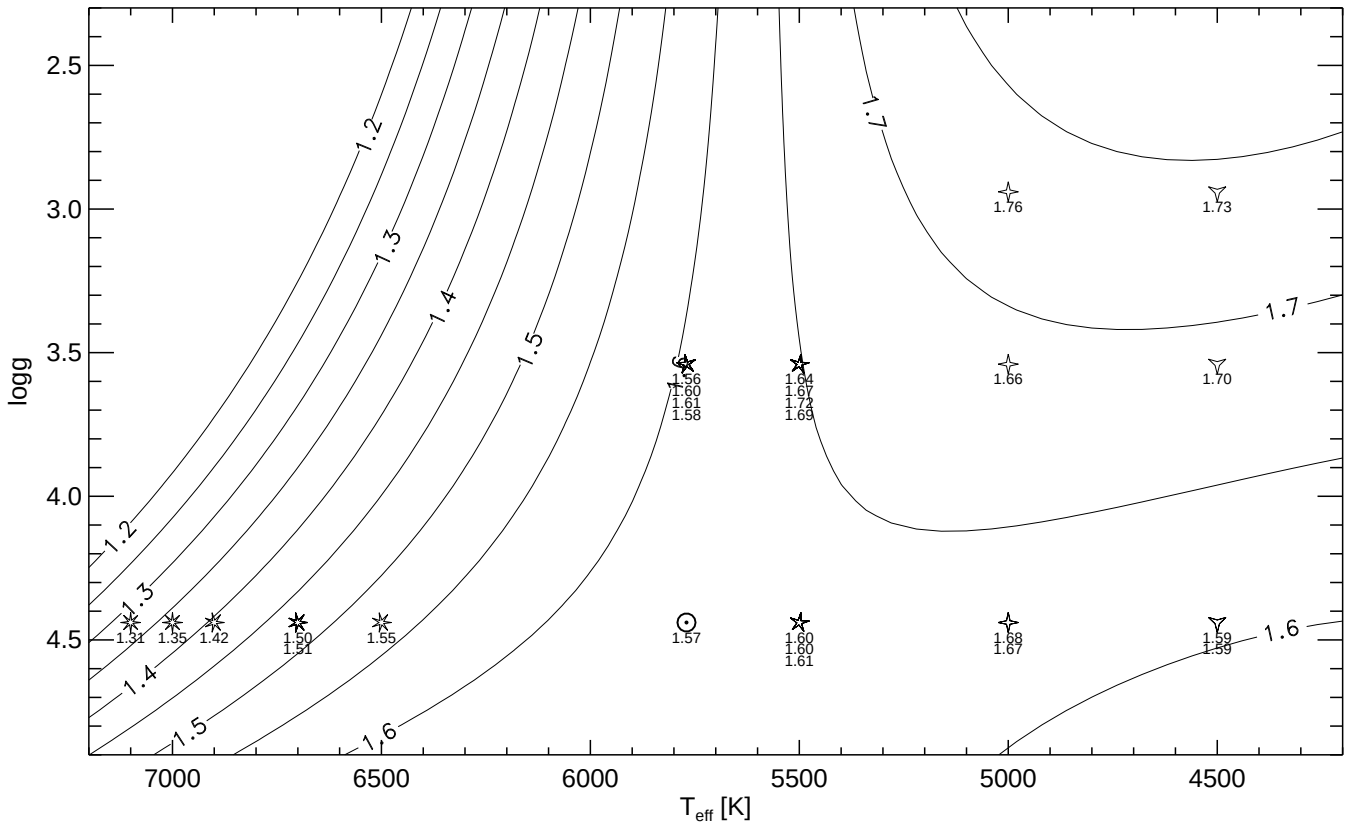

Figure 8: Calibrated parameter α for standard MLT for [M/H]=-0.5 as function of effective temperature $T_{\rm eff}$ and gravity log$g$.

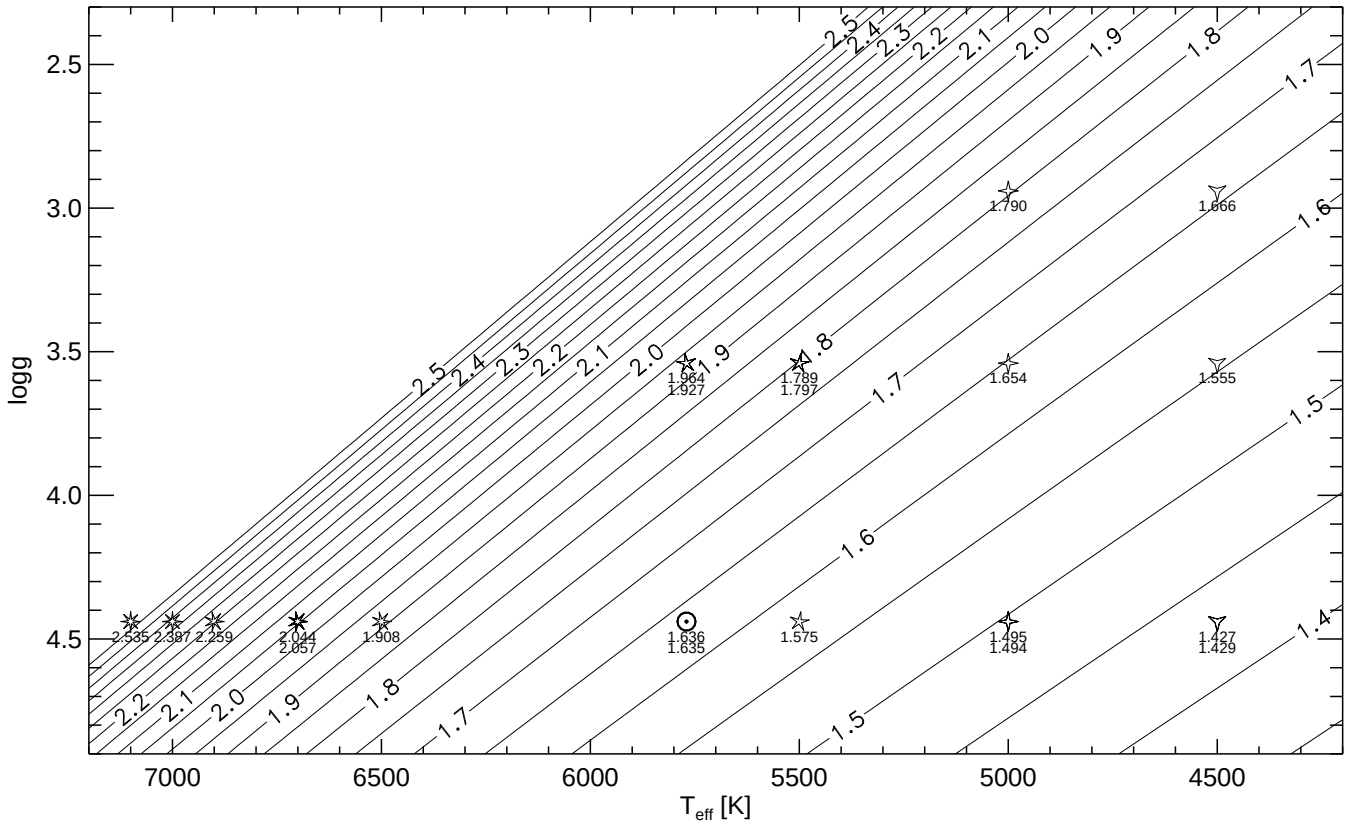

Figure 9: Entropy s^* of the adiabatic layers for [M/H]=-1.0 as function of effective temperature $T_{\rm eff}$ and gravity log$g$.

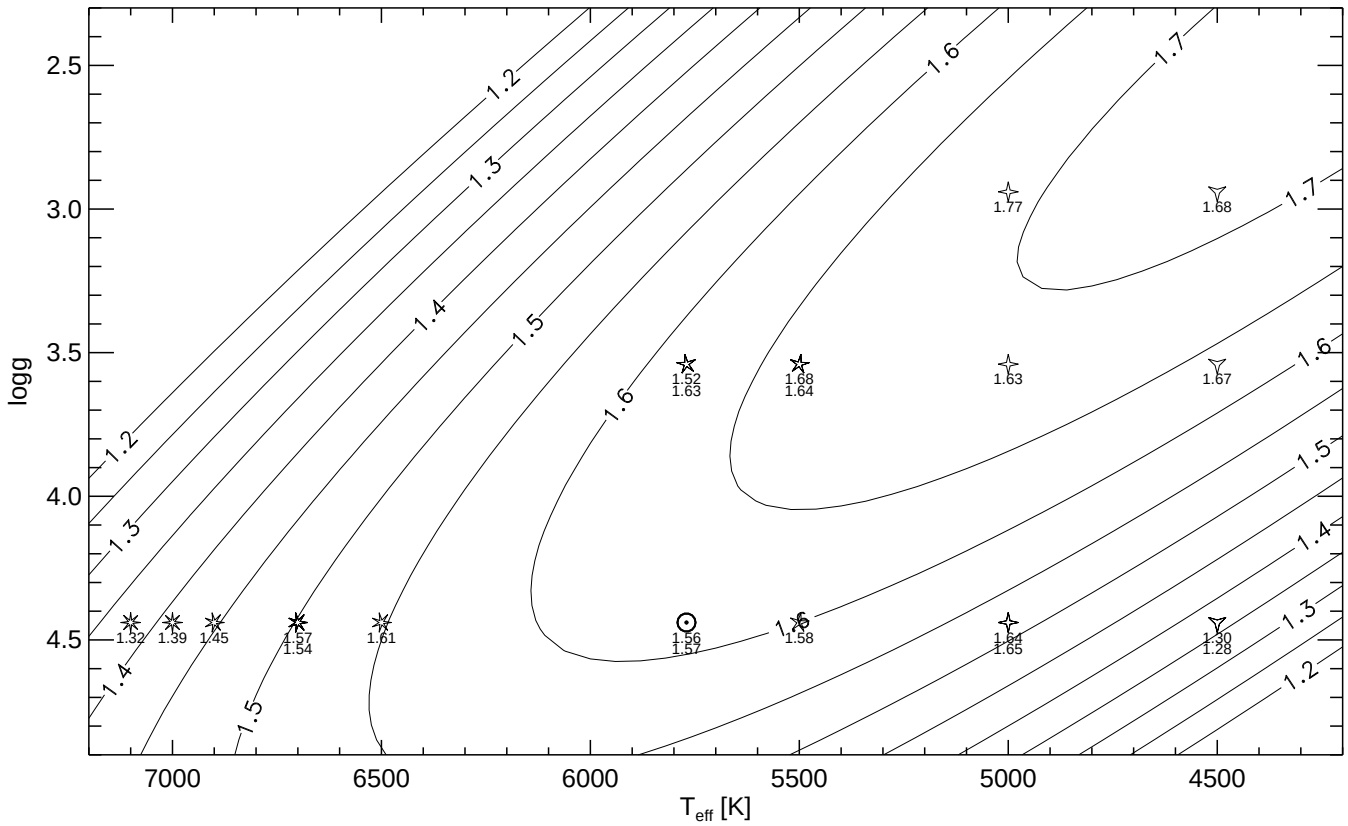

Figure 10: Calibrated parameter α for standard MLT for [M/H]=-1.0 as function of effective temperature $T_{\rm eff}$ and gravity log$g$.

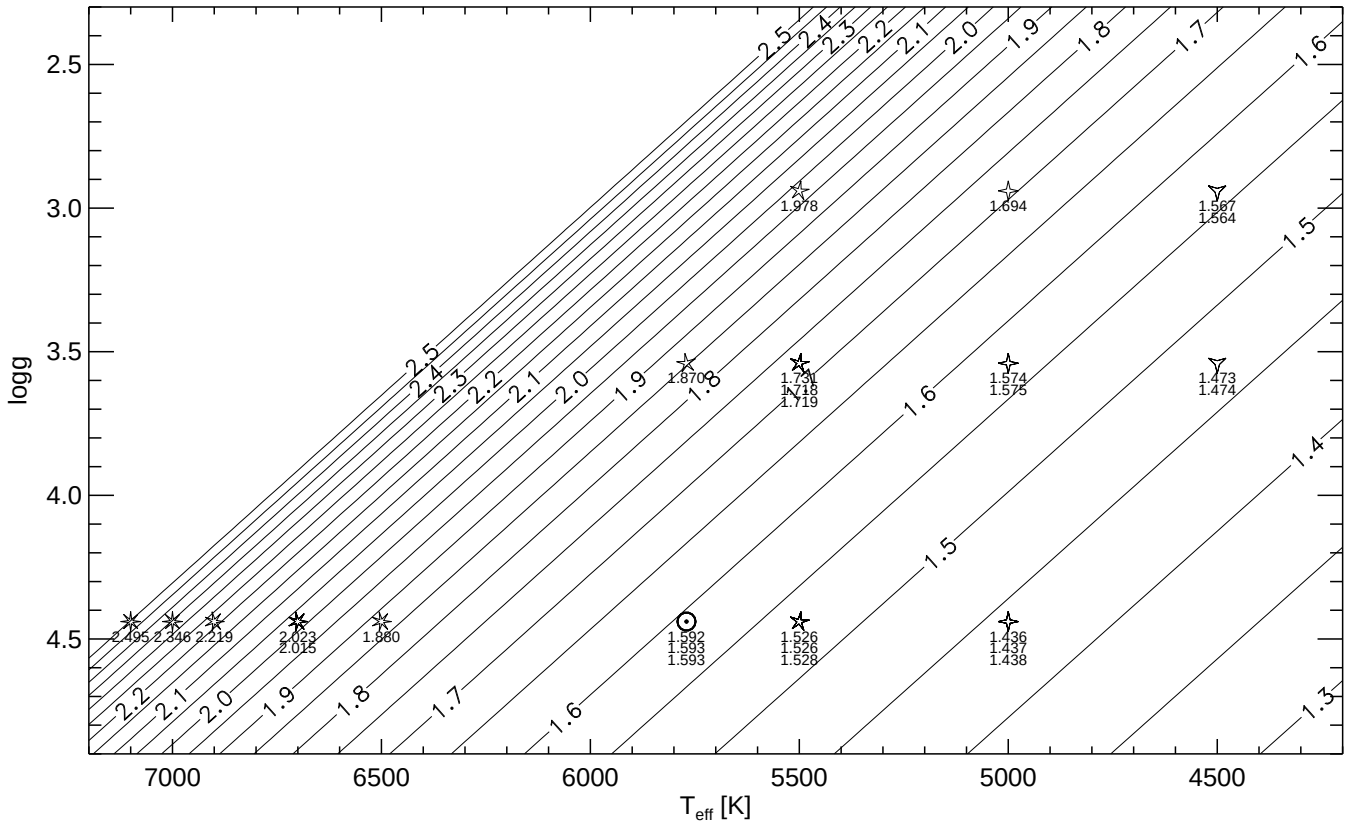

Figure 11: Entropy s^* of the adiabatic layers for [M/H]=-2.0 as function of effective temperature $T_{\rm eff}$ and gravity log$g$.

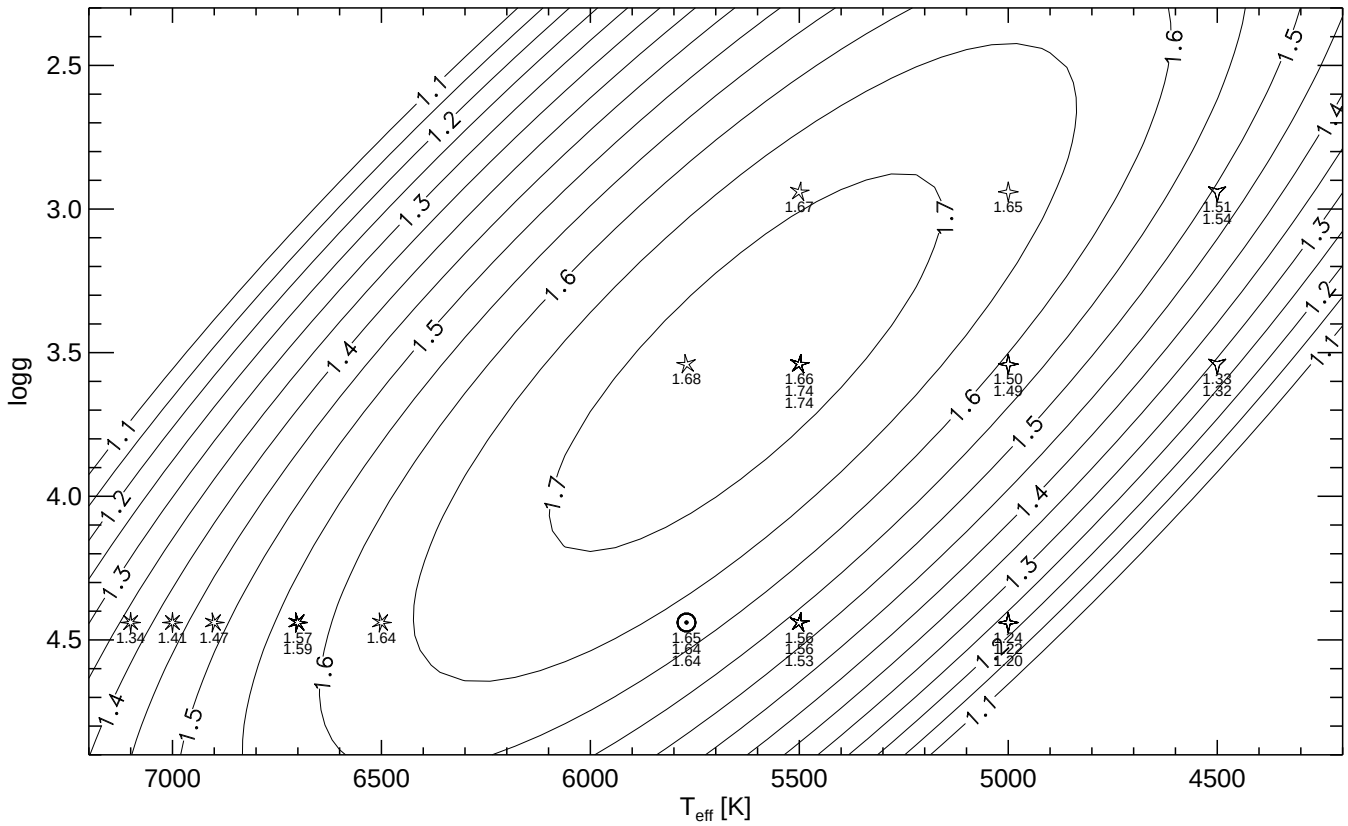

Figure 12: Calibrated parameter α for standard MLT for [M/H]=-2.0 as function of effective temperature $T_{\rm eff}$ and gravity log$g$.

5 Canuto-Mazzitelli theory with $\ell{=}\alpha H_p$ ..... ⇒

The characteristic length-scale of the Canuto-Mazzitelli theory can be calibrated in the same way as the mixing-length. With the parametrization $\ell{=}\alpha H_p$ the parameter α shows a rather regular behaviour in the $T_{\rm eff}/\log g$ plane (Figs. 13, 15, 17, 19).

For [M/H]=0.0, -0.5, -1.0 it increases monotonically with falling effective temperature and growing gravity. Its absolute value is smaller than a typical mixing-length parameter but its relative variation is larger. For the lowest metallicity it shows the same drop at low effective temperature and high gravity as in the MLT.

With this parametrization the CMT shows a behaviour very similar to that of the MLT.

6 Canuto-Mazzitelli theory with $\ell{=}z+\alpha H_{p,\mathbf{top}}$ ..... ⇒

One result of the CMT with the parametrization $\ell{=}z+\alpha H_{p,\rm top}$ (Figs. 14, 16, 18, 20) is that strong convection becomes even more and weak convection less efficient than in the MLT.

For solar metallicity this accounts for the increase of the mixing-length parameter with falling effective temperature (compare Figs. 6 and 14) and results in a wide region in the solar-neighbourhood of the $T_{\rm eff}/\log g$ plane where the free parameter of the CMT is a constant close to 0.4.

But at both bounds of our temperature range the compensation is too strong leading to an increase of α at the high-temperature side and a strong drop at the low-temperature end.

For [M/H]=-2.0 this drop is so strong that only *negative values* of α can account for the RHD results. For this metallicity the "plateau" of approximately constant α is rather narrow. And the "plateau" value of α increases with decreasing metallicity.

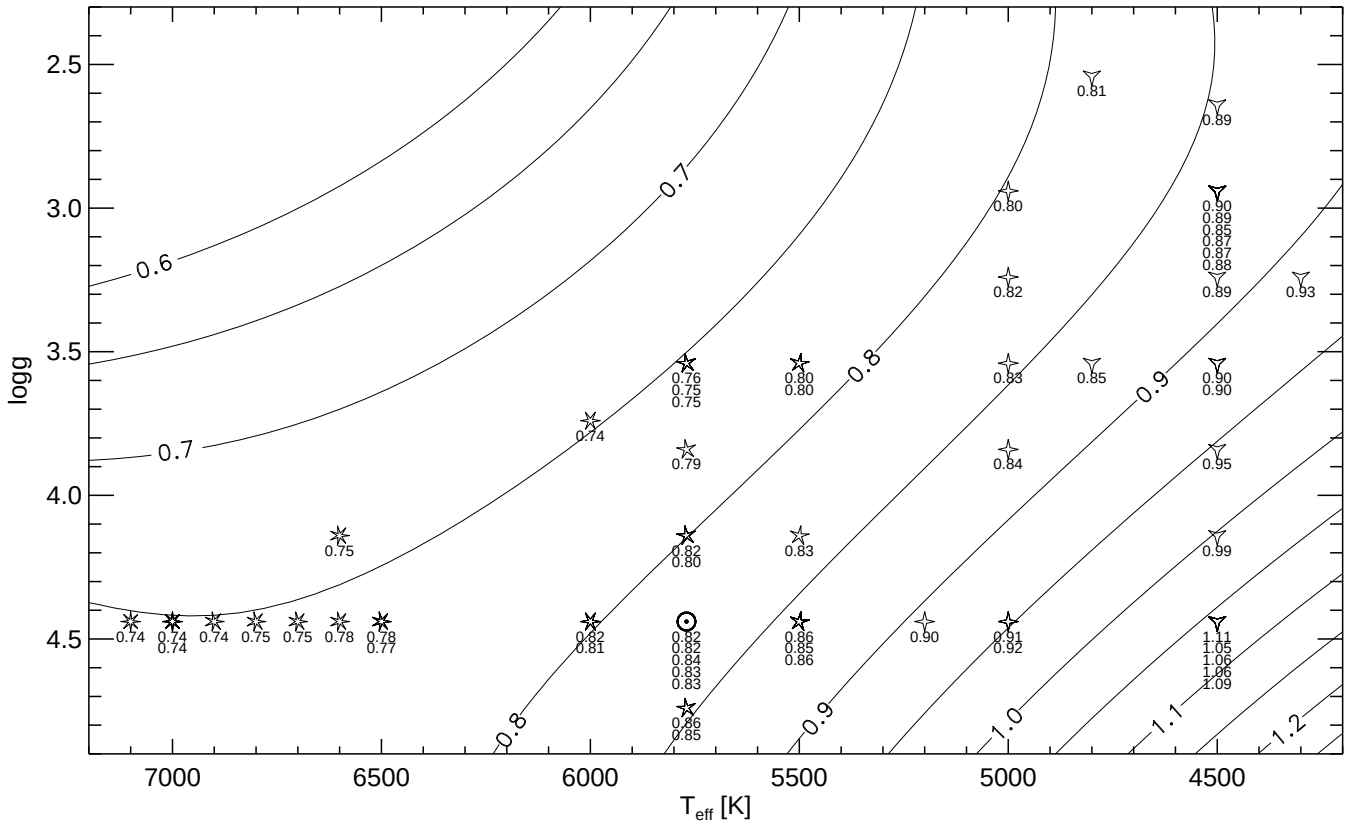

Figure 13: Calibrated parameter α for CMT($\ell{=}\alpha H_p$) for [M/H]=0.0 as function of effective temperature $T_{\rm eff}$ and gravity log$g$.

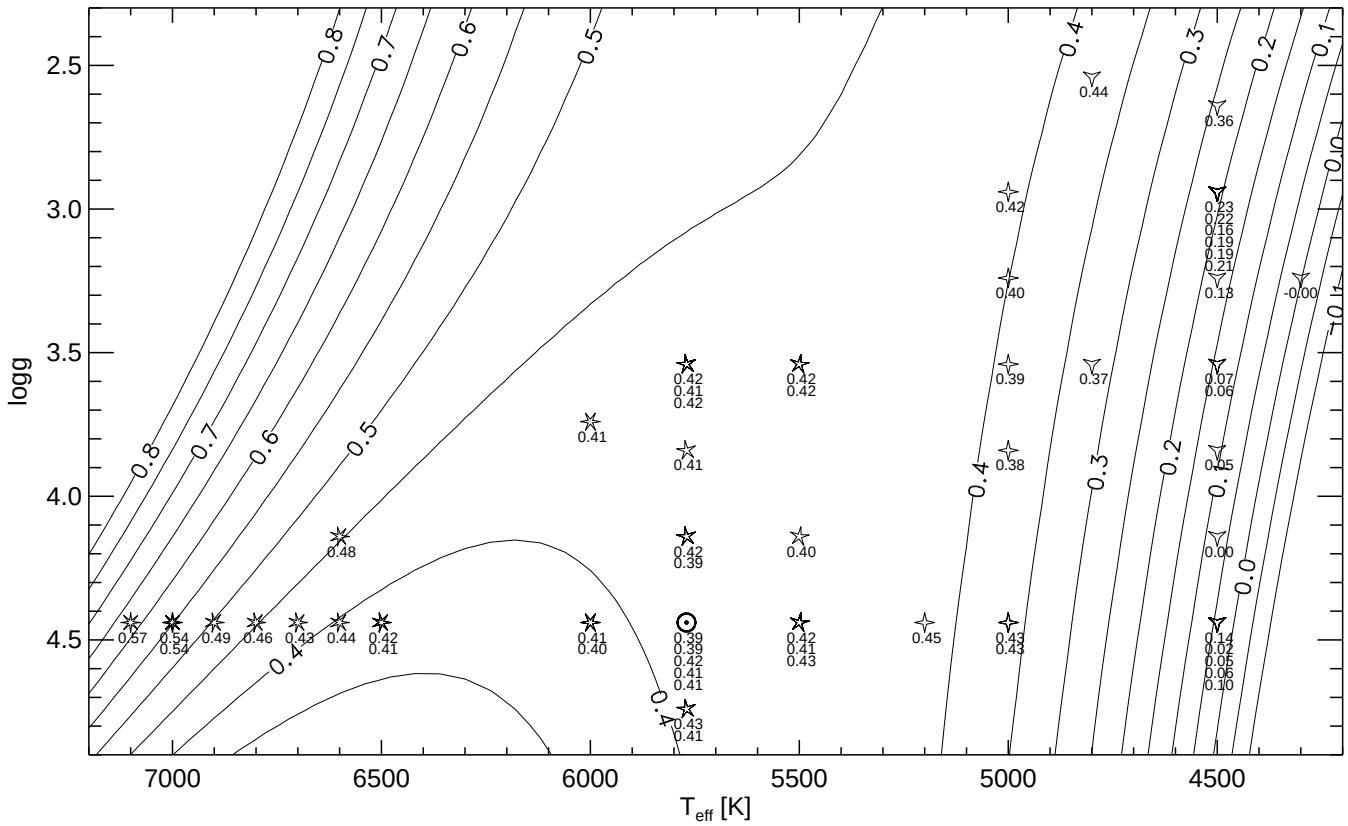

Figure 14: Calibrated parameter α for CMT($\ell{=}z+\alpha H_{p,\rm top}$) for [M/H]=0.0 as function of effective temperature $T_{\rm eff}$ and gravity log$g$.

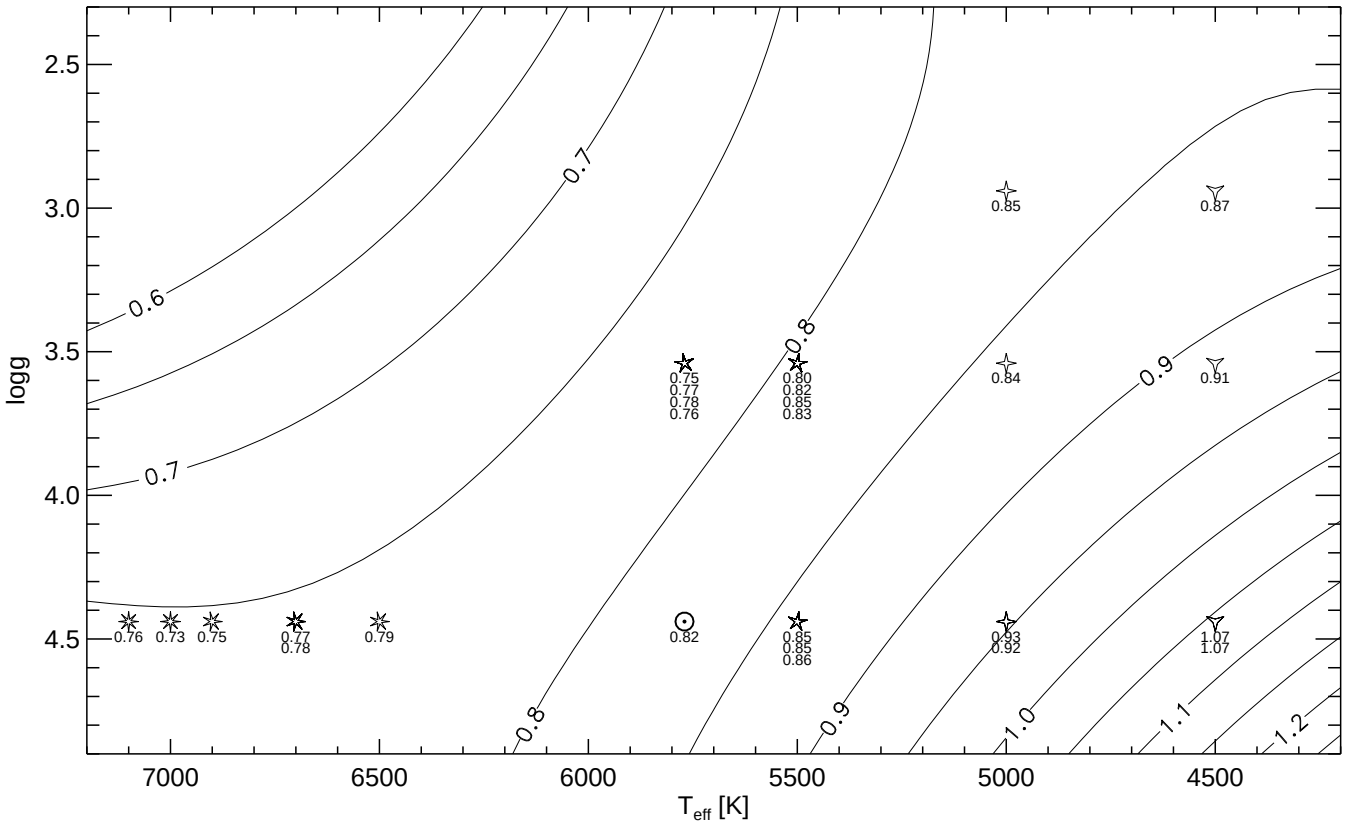

Figure 15: Calibrated parameter α for CMT($\ell{=}\alpha H_p$) for [M/H]=-0.5 as function of effective temperature $T_{\rm eff}$ and gravity log$g$.

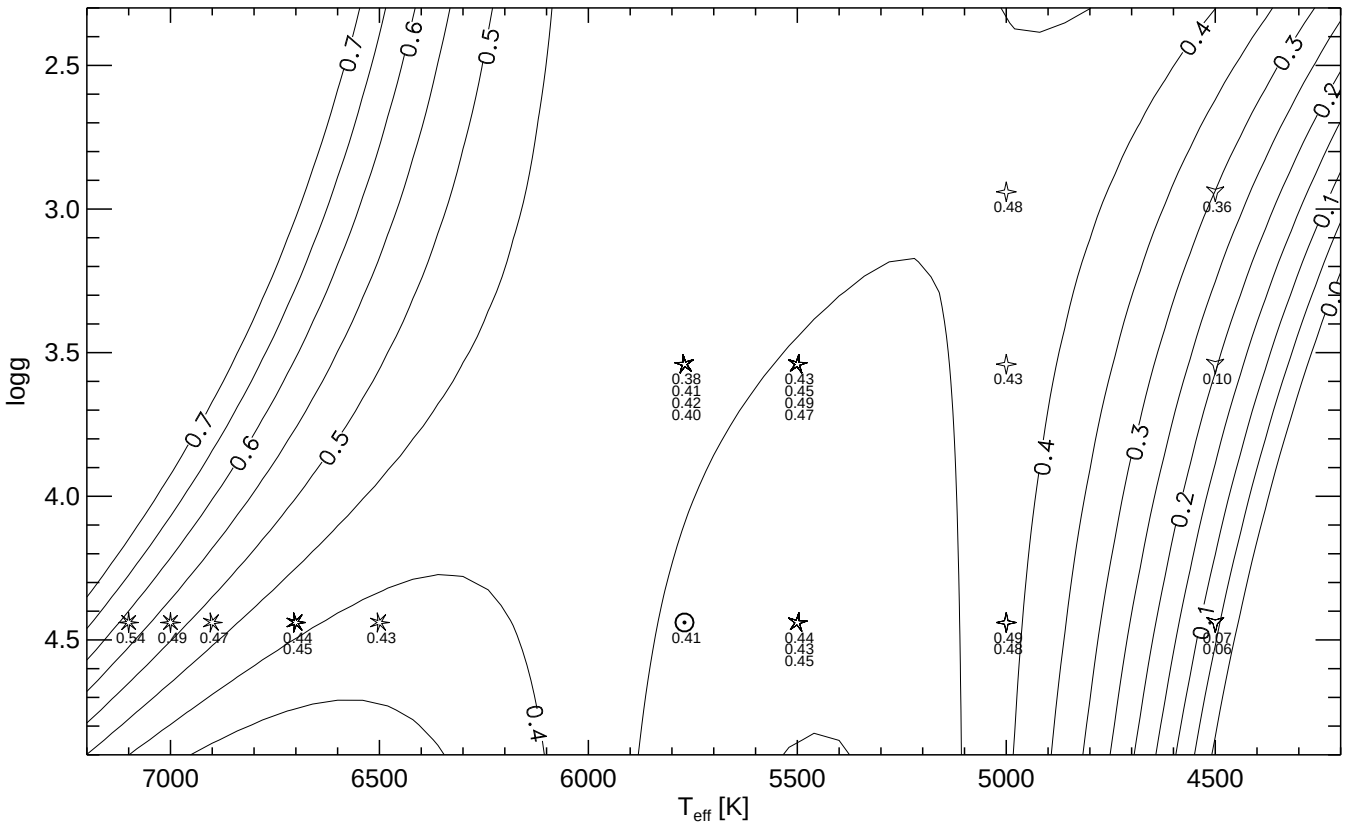

Figure 16: Calibrated parameter α for CMT($\ell{=}z+\alpha H_{p,\rm top}$) for [M/H]=-0.5 as function of effective temperature $T_{\rm eff}$ and gravity log$g$.

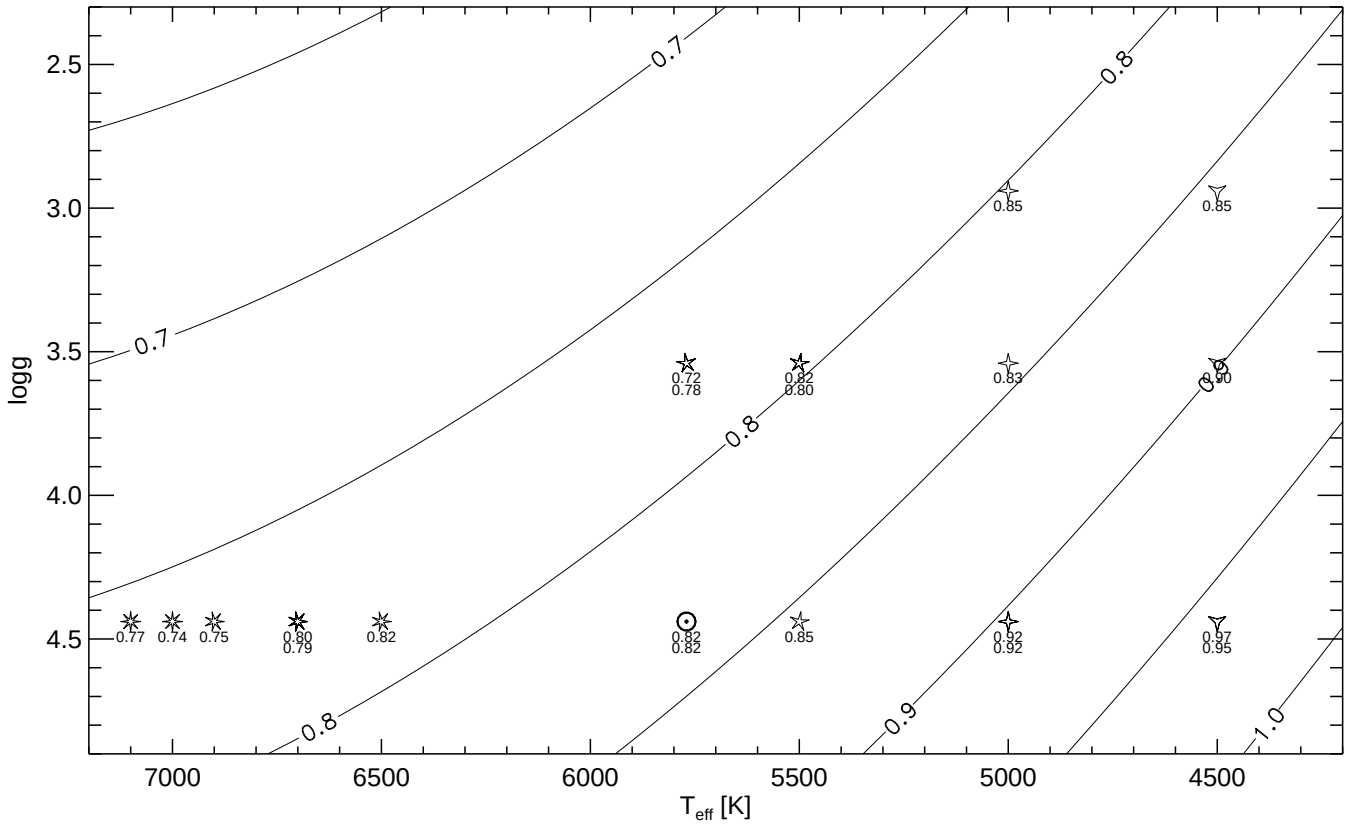

Figure 17: Calibrated parameter α for CMT($\ell{=}\alpha H_p$) for [M/H]=-1.0 as function of effective temperature $T_{\rm eff}$ and gravity log$g$.

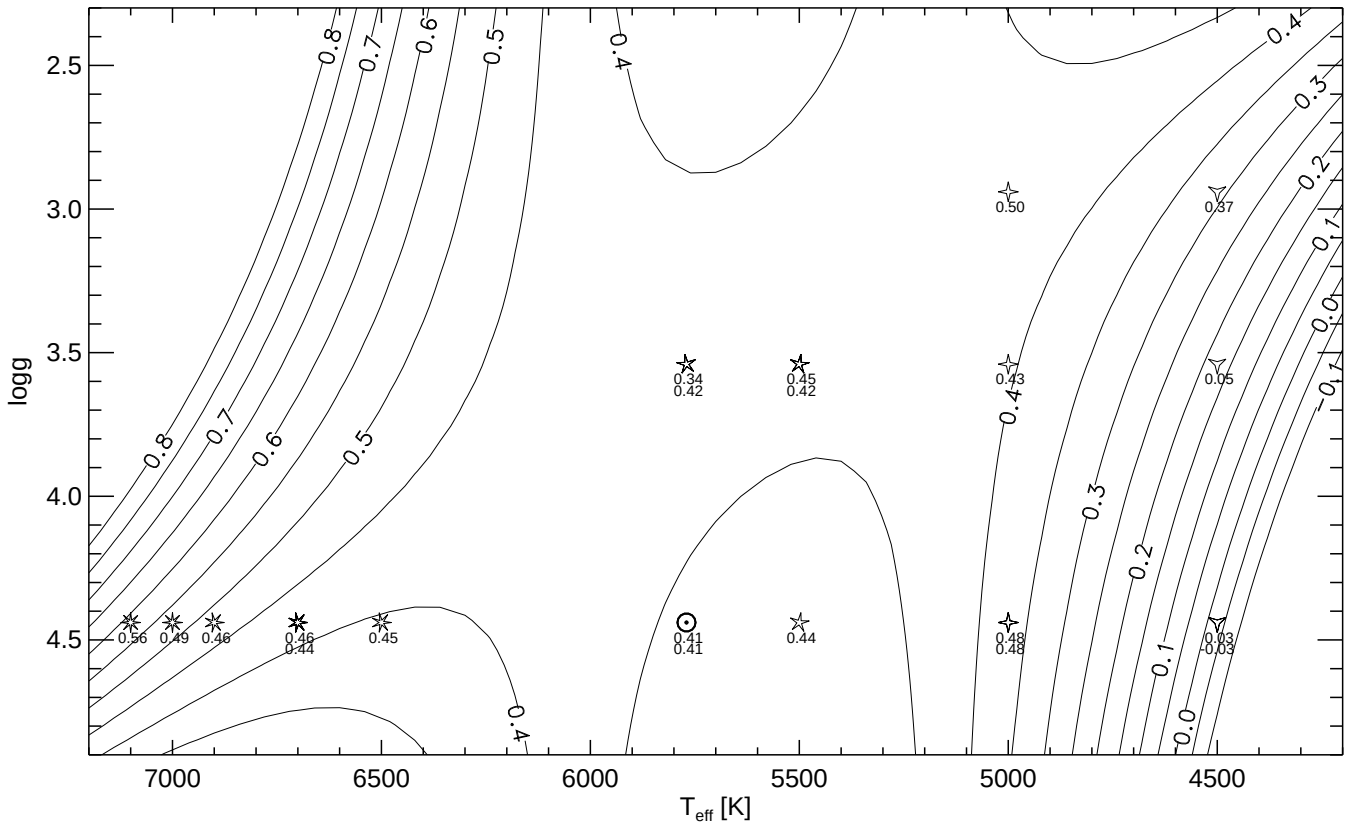

Figure 18: Calibrated parameter α for CMT($\ell{=}z+\alpha H_{p,\rm top}$) for [M/H]=-1.0 as function of effective temperature $T_{\rm eff}$ and gravity log$g$.

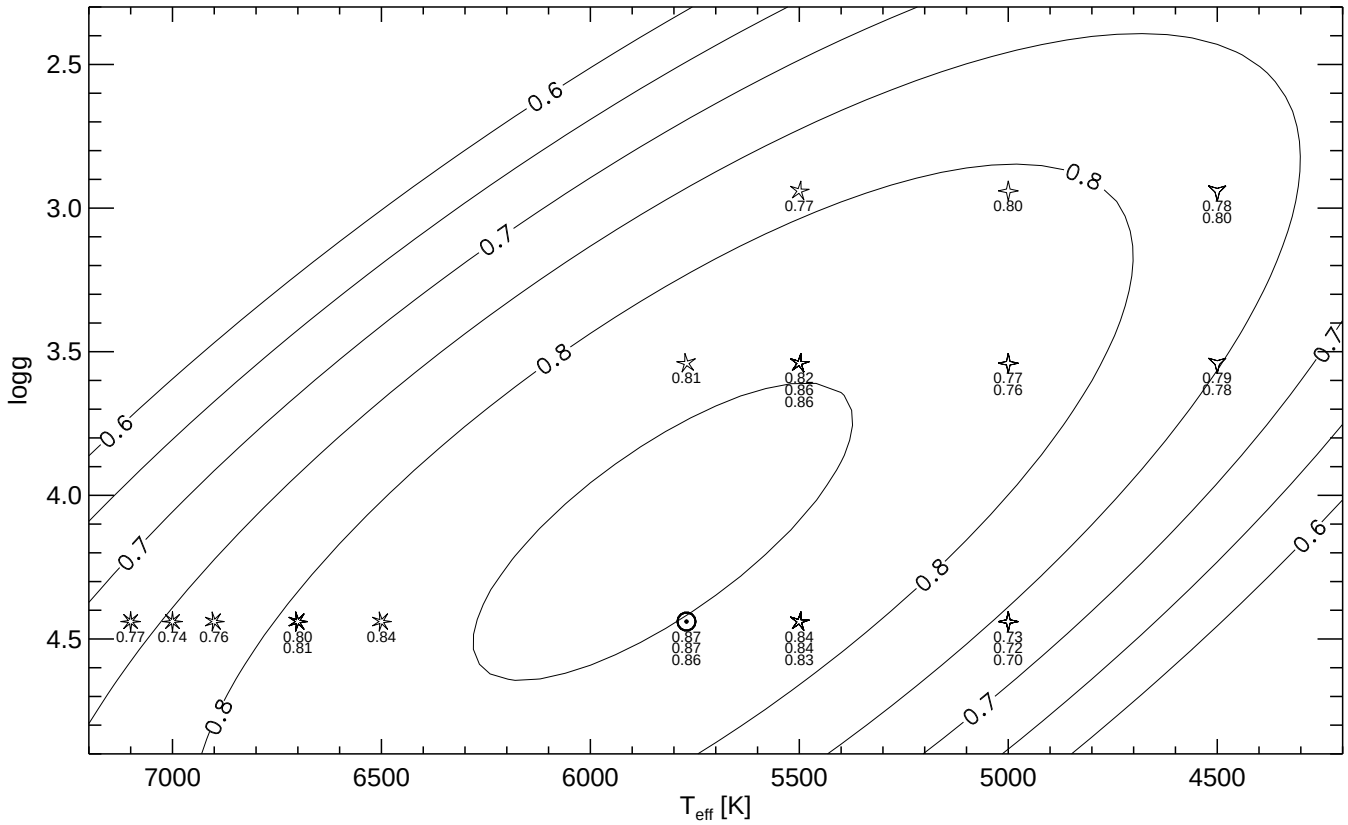

Figure 19: Calibrated parameter α for CMT($\ell{=}\alpha H_p$) for [M/H]=-2.0 as function of effective temperature $T_{\rm eff}$ and gravity log$g$.

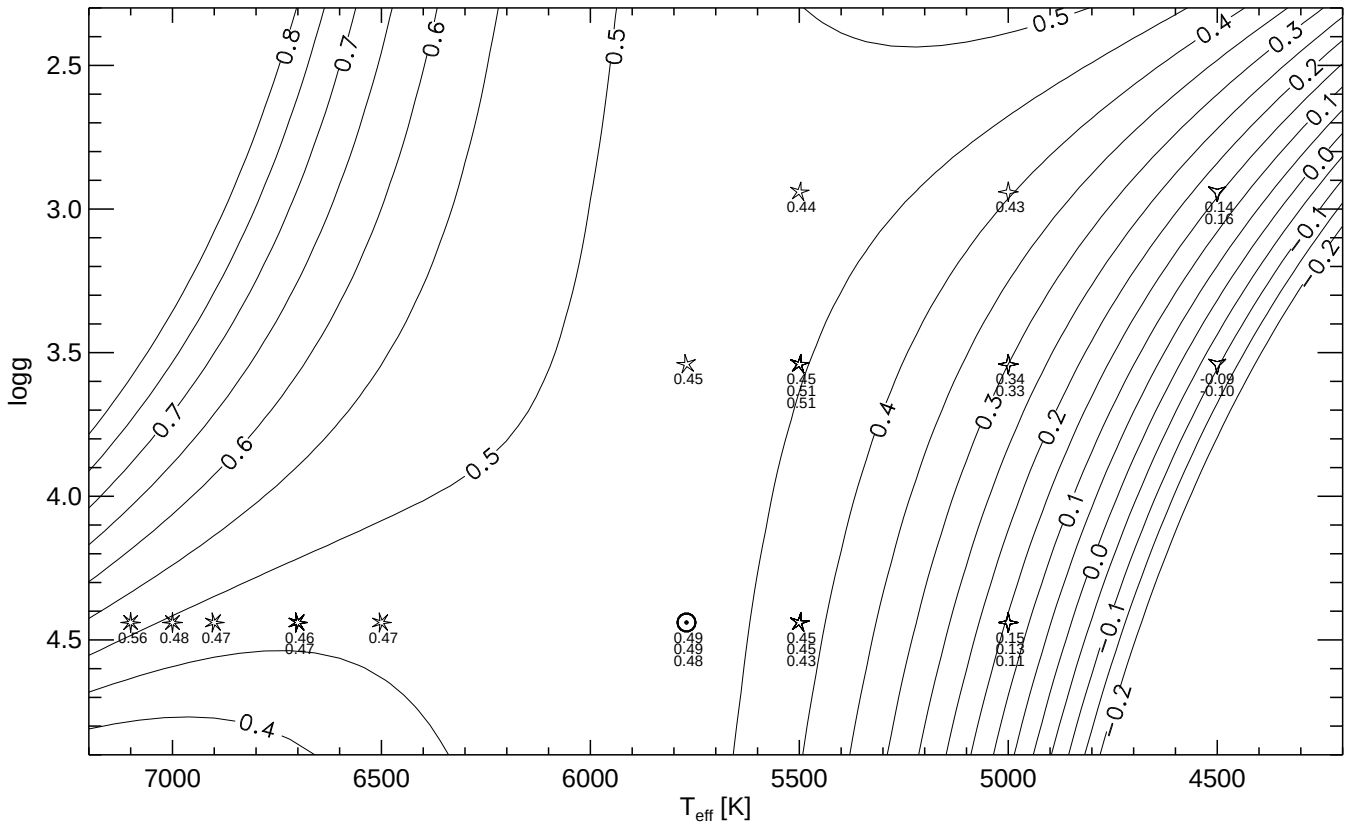

Figure 20: Calibrated parameter α for CMT($\ell{=}z + \alpha H_{p,\rm top}$) for [M/H]=-2.0 as function of effective temperature $T_{\rm eff}$ and gravity log$g$.